J. Synchrotron Rad. (1995). **2**, 163–173

Perfect Crystals in the Asymmetric Bragg Geometry as Optical Elements for Coherent X-ray Beams

S. Brauer,[a]* G. B. Stephenson[a] and M. Sutton[b]

[a]IBM Research Division, Thomas J. Watson Research Center, PO Box 218, Yorktown Heights, New York 10598, USA, and [b]Department of Physics, McGill University, Rutherford Building, 3600 University Street, Montréal, Québec, Canada H3A 2T8

(*Received 24 August 1994; accepted 3 March 1995*)

Perfect crystals in the asymmetric Bragg geometry are evaluated as optical elements for manipulating coherent X-ray beams. Such optics can be used to modify the transverse coherence length of a synchrotron X-ray beam, with the intention of increasing the usable coherent flux. The wavelength range, angular divergence and flux of X-rays passing through a pinhole aperture are examined in detail, as functions of source and pinhole size, crystal-to-pinhole separation and the asymmetry factor. In developing this analysis, the behavior of asymmetrically cut crystals is explained in reciprocal space, with reference to the crystal truncation rod associated with the reflection. The results show that, for synchrotron beams that are collimated to a small fraction of the incident Darwin width, the wavelength range accepted by the crystal is typically dispersed into an angular spread in the exit beam. This chromatic aberration greatly reduces the transverse coherence length in a manner that does not conserve the coherent flux. The calculations are in agreement with measurements of the divergence and flux through a micrometer-sized pinhole using a synchrotron wiggler X-ray source.

Keywords: perfect-crystal optics; coherent X-ray beams; coherent flux; dynamical diffraction; crystal truncation rod.

1. Introduction

Understanding the behavior of perfect crystals as X-ray optical elements is becoming increasingly important as the collimation of synchrotron X-ray sources increases. In the past, the angular divergence of the source was generally significantly larger than the angular acceptance (Darwin width) of a crystal monochromator. In contrast, the divergence of the beam emitted by an X-ray undulator at a third-generation synchrotron (~20 μrad) is smaller than the Darwin width of a typical monochromator crystal. Under these new conditions, it is necessary to understand the detailed optical behavior of diffracting crystals, such as the exact angles the exit beam makes with respect to the incident beam, on a scale finer than the Darwin width. These properties are especially important for the manipulation of *coherent* X-ray beams, which have typically been collimated to a small fraction of the total source divergence.

The use of coherent X-ray beams is a new area of research in X-ray science, made feasible by recent large increases in the brilliance of X-ray sources. This development is exciting because many powerful experimental techniques that rely on coherent illumination have previously been limited to visible wavelengths, where high-brilliance sources (*e.g.* lasers) are available. Such techniques can now be considered at hard-X-ray wavelengths. With advantage taken of the small wavelength and relatively large penetration depth, X-ray speckle patterns from antiphase domains in a binary metal alloy have already been observed (Sutton *et al.*, 1991). Techniques such as X-ray intensity-fluctuation spectroscopy (XIFS) and Fourier imaging of atomic sized structures with coherent X-rays are currently under development (Dufresne *et al.*, 1992; Brauer, Stephenson, Sutton, Brüning *et al.*, 1995). For each of these techniques it is essential to obtain the maximum coherent flux, and to control the spatial and angular size and the wavelength content of the coherent beam. In this paper, we will focus on the use of asymmetrically cut perfect crystals to influence these properties of the X-ray beam.

Although synchrotron sources emit incoherent radiation, coherent X-ray illumination may be obtained by selecting a sufficiently collimated and monochromatic portion of the light. The longitudinal coherence length d_l is determined by the range of wavelengths $\Delta\lambda$ through the relation $d_l = \lambda^2/2\Delta\lambda$. A typical symmetrically cut Si(111) monochromator gives $\Delta\lambda/\lambda \simeq 1.3\times10^{-4}$, so that the longitudinal coherence length is about 0.3 μm for $\lambda =$ 0.10 nm. The transverse coherence length d_t is determined by the divergence D through the relation $d_t = \lambda/2D$. In the absence of optical elements which affect the collimation, the divergence at a point is equal to the angle subtended by the source. At a distance $L = 30$ m from a source of size $A = 300$ μm one obtains $D = A/L \simeq 10$ μrad, which gives $d_t \simeq 5$ μm. A pinhole aperture several micrometers

* Present address: Advanced Photon Source, Argonne National Laboratory, Argonne, IL 60439, USA.

in diameter serves to select a portion of the beam which is transversely coherent, discarding most of the incident radiation. Since the coherent flux is proportional to the brilliance of the source, high-brilliance insertion devices are required to obtain sufficient coherent flux for most experiments.

Our main motivation for this work is to increase the usable coherent flux from synchrotron sources. For experiments such as XIFS, there is an optimum size for the transverse coherence length which depends upon the length scales of interest in the sample. In our experiments, transverse coherence lengths of one micrometer or less are often sought. Since the transverse coherence length of the raw beam from an insertion device source is typically larger than this, the ability to modify the transverse coherence length without loss of coherent flux is in general very desirable. In addition, control of the longitudinal coherence length is required.

The spatial size of synchrotron sources is typically larger horizontally than vertically, often by a factor of 10. Thus, the collimation is better, and the transverse coherence length is larger in the vertical direction than the horizontal. If a circular pinhole aperture is used to select a coherent beam, it must have a diameter approximately equal to the smaller of the two transverse coherence lengths. In this configuration, only one tenth of the vertical transverse coherence length is admitted and 90% of the coherent flux is discarded. Although elliptical apertures could be used, a symmetric coherence volume is better suited to many experiments. In our XIFS experiments, for example, equal transverse coherence lengths are well matched to the isotropic antiphase domains within the samples.

The full brilliance of such an asymmetric source would be better exploited if optical elements were used to match the vertical coherence length with the horizontal whilst preserving the coherent flux. For example, a focusing optic such as an X-ray mirror could be used to trade off vertical collimation for increased flux per unit area. However, in practice, a glancing incidence X-ray mirror can be inconvenient because of its expense and because it must be situated far upstream of the experiment to provide the optimum geometry. In this article, we consider the use of asymmetrically cut crystals to perform this function. Such crystals have fundamentally different optical properties than focusing mirrors. In particular, we have studied an Si(111) crystal cut to condense the beam spatially by 10× in the vertical direction. We have measured the resulting increase in vertical divergence in order to determine the vertical coherence length produced. Our measurements on the X25 wiggler beamline at the National Synchrotron Light Source (NSLS) are explained by calculations of the wavelength–angle–position correlations in the optical system.

We note that asymmetrically cut crystals have previously been used to manipulate coherent X-ray beams, with the rather different intention of increasing the coherence volume at the expense of useful coherent flux (Ishikawa, 1988).

2. The asymmetric Bragg geometry – overview

We briefly review the behavior of asymmetrically cut perfect crystals in the Bragg (reflection) geometry. More extensive reviews are provided by Matsushita & Hashizume (1983) and Caciuffo, Melone, Rustichelli & Boeuf (1987). We restrict our discussion to geometries in which the surface normal of the crystal is in the diffraction plane, so that 'inclined' geometries are not considered. Although much of the analysis developed here applies, a discussion of the Laue (transmission) and inclined Bragg cases is deferred to subsequent publications (*e.g.* Brauer, Stephenson, Sutton, Mochrie *et al.*, 1995).

The asymmetric Bragg geometry is shown in Fig. 1, where the diffracting lattice planes form an angle α with the crystal surface. Just as in the symmetric case ($\alpha = 0$), when the diffraction conditions are met, the angles between the reflecting lattice planes and both the incidence and exit beams are approximately equal to the Bragg angle θ_B. For a crystal of lattice spacing d, the Bragg angle for a wavelength λ is given by

$$\theta_B \equiv \sin^{-1}(\lambda/2d), \tag{1}$$

and is sometimes called the kinematical Bragg angle. The exact angles of the incident and exit beams with respect to the surface of the crystal may be expressed as

$$\theta_i = \theta_B + \alpha + \Delta\theta_i, \tag{2}$$

$$\theta_e = \theta_B - \alpha + \Delta\theta_e, \tag{3}$$

where $\Delta\theta_i$ and $\Delta\theta_e$ are the small deviations of the incident and exit beam directions, respectively, from the Bragg-law directions. These deviations arise because of both the finite width of the reflection (the Darwin width) and a correction arising from the index of refraction within the crystal. The deviations are always very small (<100 μrad). For a perfect crystal with a flat surface, there is an exact one-to-one relationship between the incidence and exit angles for a given wavelength, which we will discuss shortly.

The asymmetry of the surface orientation can be characterized by an asymmetry factor

$$b \equiv \frac{\sin(\alpha + \theta_B)}{\sin(\alpha - \theta_B)}. \tag{4}$$

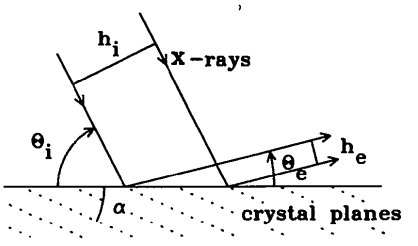

Figure 1
Reflection geometry for diffraction from an asymmetrically cut perfect crystal.

For the Bragg geometry, where α is smaller than θ_B, θ_e is positive and b is negative. For a given crystal having fixed values of α and d, the parameter b depends implicitly on wavelength through θ_B. The value $b = -1$ represents the symmetric Bragg case ($\alpha = 0$), whilst $b = 1$ represents the symmetric Laue case ($\alpha = \pi/2$).

Several features of diffraction from asymmetrically cut crystals can be understood by considering perfectly monochromatic illumination. First, as seen from the geometry of Fig. 1, the spatial width of the beam in the diffraction plane is altered by a geometrical 'foreshortening' effect according to

$$h_e = h_i/|b|, \tag{5}$$

where h_i and h_e are the spatial extent of the incident and exit beams, respectively. In the geometry of Fig. 1, $|b| > 1$ so that the radiation is spatially condensed and the flux per unit area of the reflected beam is increased. The crystals used in our measurements were cut to give $|b| = 10$ at the operating wavelength.

The second feature which contrasts the asymmetric with the symmetric case is that the beam divergence in the diffraction plane is altered upon reflection from an asymmetrically cut crystal. General expressions for the exact incidence and exit angles over which reflection occurs, derived from dynamical diffraction theory, will be given in the next section. One simple result is the relationship between $\Delta\theta_i$ and $\Delta\theta_e$, given by

$$\Delta\theta_e = -b\,\Delta\theta_i. \tag{6}$$

It follows that for a monochromatic beam containing a range of incident angles that are *all* reflected from the crystal, the exit divergence is $|b|$ times as large as the incident divergence. For $|b| > 1$ the reduction in collimation is the price paid for spatially condensing the beam. The effect is especially important for coherent X-ray studies since the increased divergence decreases the transverse coherence length.

With these general ideas about diffraction from asymmetrically cut perfect crystals under monochromatic illumination, two questions arise in the context of our application. First, if we illuminate such a crystal with polychromatic radiation, exactly what wavelengths and angles will be transmitted through a pinhole aperture in the diffracted beam? These factors will determine the observed longitudinal and transverse coherence lengths. Secondly, how much might we expect the usable coherent flux to be increased in an asymmetric geometry? To answer these questions analytically, we use the next section to present the detailed behavior of a crystal in the asymmetric Bragg geometry, as derived from dynamical diffraction theory. In subsequent sections we employ two established formalisms for following the wavelength, angle and position of rays through our optical system. Thereafter, we consider the implications for coherent beam experiments.

3. Results of dynamical diffraction theory for the asymmetric Bragg geometry

The exact relationship between the incident and exit beam directions, and the expression for the reflectivity as a function of incident beam direction, can be obtained as a function of wavelength and crystal parameters by using dynamical diffraction theory. We will demonstrate how the results of dynamical diffraction theory for a flat perfect crystal can be concisely described in reciprocal space using the concept of a crystal truncation rod (CTR). The relationship between the CTR and the dispersion surface representation of Batterman & Cole (1964) is described in more detail in the *Appendix*.

Let us briefly review some key results of dynamical diffraction theory, following the classic review paper by Batterman & Cole (1964). Neglecting absorption, for a semi-infinite centrosymmetric crystal, the ratio of the brilliance of the exit beam B_e (photons per unit time per unit solid angle per unit area per unit wavelength range) to that of the incident beam B_i can be expressed as

$$\frac{B_e(\theta_e,\lambda)}{B_i(\theta_i,\lambda)} = |\eta - (\eta^2 - 1)^{1/2}|^2, \tag{7}$$

where η is a normalized angular deviation defined in terms of $\Delta\theta_i$ by the relation

$$\eta \equiv \frac{\Delta\theta_i - \Delta\theta_i^{\rm cen}}{w_i}. \tag{8}$$

The function B_e/B_i given in (7) is centered at $\eta = 0$ and has a value of unity for the range $-1 \le \eta \le 1$. One can see from (8) that for monochromatic radiation, in terms of the incidence angle, the full width of the reflection (the incident Darwin width) is $2|w_i|$ while the center of the reflection is offset by $\Delta\theta_i^{\rm cen}$ from the Bragg-law angle. (Although the actual FWHM is $2.12|w_i|$, the effect of absorption, which we have neglected, is to make the peak slightly narrower. We will simply use $2|w_i|$ as the full width.) The dynamical theory gives

$$w_i = \tan\theta_B P \frac{|b|^{1/2}}{b} \Psi_H, \tag{9}$$

$$\Delta\theta_i^{\rm cen} = \tan\theta_B \frac{|F_0|}{|F_H|} \frac{b-1}{2b} \Psi_H, \tag{10}$$

where $P = 1$ for σ polarization, $P = |\cos 2\theta_B|$ for π polarization, and $|F_0|$ and $|F_H|$ are the magnitudes of the structure factors per unit cell for the (000) and **H** reflections, respectively. The dimensionless parameter Ψ_H (introduced here) is particularly useful since it is *independent of wavelength*, and is characteristic of a given reflection from a crystal. It is defined by

$$\Psi_H \equiv \frac{2r_e}{\pi} \frac{d^2|F_H|}{V}, \tag{11}$$

where $r_e \equiv e^2/mc^2 = 2.8\times10^{-13}$ cm is the Thompson electron radius and V is the unit-cell volume. The half width and offset of the exit-angle deviation are simply related to

those of the incidence angle by the expressions

$$w_e = -b\,w_i \tag{12}$$

$$\Delta\theta_e^{\rm cen} = -b\,\Delta\theta_i^{\rm cen} \tag{13}$$

which are similar to (6). In the Bragg case, both w_i and w_e are negative numbers while $\Delta\theta_i^{\rm cen}$ and $\Delta\theta_e^{\rm cen}$ are positive.

Typical values of d, $|F_0|/|F_H|$ and Ψ_H are shown in Table 1 for a selection of crystal reflections. In the specific case of $\lambda = 0.177$ nm and σ polarization, angular widths and offsets for the same reflections are listed in Table 2, for both $b = -1$ and $b = -10$.

The above results from dynamical theory may be compactly described in reciprocal space, using the concept of a CTR, by simply extending the geometry used in deriving the dynamical theory. While the necessary geometrical construction is shown in detail in the *Appendix*, the results may be described using Fig. 2, which shows a reciprocal-space diagram for the asymmetric Bragg geometry. The incident and exit beams are indicated by vectors $\mathbf{k}_i$ and $\mathbf{k}_e$, each of length $2\pi/\lambda$. In the simple kinematical approximation, the diffraction condition would be satisfied when the scattering vector $\mathbf{q} \equiv \mathbf{k}_e - \mathbf{k}_i$ is equal to the reciprocal lattice vector $\mathbf{H}$ of the diffracting planes, which has a length $2\pi/d$. As described in the *Appendix*, the permitted scattering vectors in dynamical theory are those which terminate along the line passing through the point H and oriented perpendicular to the crystal surface. In a general sense, this line is the CTR associated with the reciprocal lattice point H. Commonly discussed from a kinematical approach (Robinson, 1986), such CTRs arise in the diffraction pattern of a crystal which is truncated by a crystal.

To maintain $\mathbf{q}$ on the line of the CTR, the incidence and exit angles must satisfy the relationship

$$(\lambda/d)\sin\alpha = \cos\theta_e - \cos\theta_i. \tag{14}$$

This result is required for momentum conservation as was shown by Kuriyama & Boettinger (1975). When $\alpha = 0$ we find $\theta_i = \theta_e$ as expected. However, for $\alpha \neq 0$, the incidence and exit angles are related in a manner which depends upon the wavelength. Note that differentiation of (14) at constant wavelength leads to (6).

Dynamical theory predicts that the crystal exhibits near-unit reflectivity only over the range $-1 \leq \eta \leq 1$. In reciprocal space, scattering vectors corresponding to this range all terminate on a small segment of the CTR labeled T in Fig. 2. The region T is slightly displaced from $\mathbf{H}$ because the index of refraction within the crystal is slightly less than one. The length of T is inversely proportional to the extinction depth of X-rays in the crystal, as determined by dynamical theory. From the geometry detailed in the *Appendix*, it can be shown that the line segment T has a length $2|w_i S|$ and its center is shifted from $\mathbf{H}$ along the CTR by an amount $\Delta\theta_i^{\rm cen} S$, where

$$S = \frac{\pi}{d}\frac{\sin 2\theta_{\rm B}\cos 2\alpha}{\sin\theta_{\rm B}\sin(\theta_{\rm B}-\alpha)}. \tag{15}$$

Table 1
Parameters used to calculate the angular widths w_i, w_e and angular offsets $\Delta\theta_i^{\rm cen}$, $\Delta\theta_e^{\rm cen}$ for various crystal reflections.

	Si(111)	Si(220)	Diamond(111)
d (nm)	0.3135	0.1920	0.2059
$\lvert F_0\rvert/\lvert F_H\rvert$	1.85	1.59	2.69
Ψ_H (μrad)	66.7	29.1	29.9

4. The DuMond formalism

4.1. *Monochromatic source*

An elegant formalism for tracing the wavelengths and angles of rays diffracted by perfect crystals was put forward by DuMond (1937) more than 50 years ago. DuMond represented Bragg's law (1) graphically, similar to Fig. 3. The relationship between wavelength and angle for a diffracting crystal is shown by plotting wavelength, scaled to the crystal d spacing, as a function of incidence angle on one side, and exit angle on the other. Such a figure depicts the mapping from incidence angle to exit angle, the wavelength of the ray being unchanged. Because we are considering the Bragg geometry, in which $\theta_e > 0$, the curve is drawn as a dotted line in the region $0 < \theta_i < 2\alpha$. This region corresponds to the Laue geometry which we will discuss in another work (Brauer, Stephenson, Sutton, Mochrie *et al.*, 1995). Obviously, the incidence and exit curves become symmetric about the origin if the crystal is symmetrically cut ($\alpha = 0$).

The curves shown on the DuMond diagram have the form

$$\lambda/2d = \sin(\theta_i - \alpha - \Delta\theta_i), \tag{16}$$

$$\lambda/2d = \sin(\theta_e + \alpha - \Delta\theta_e), \tag{17}$$

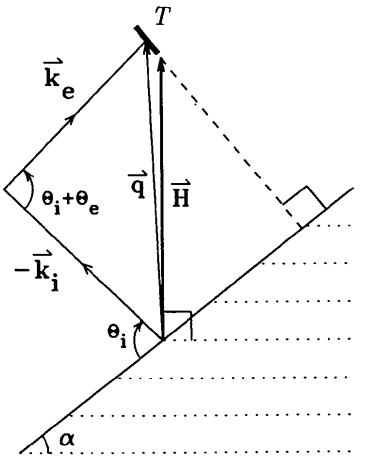

Figure 2
Reciprocal-space representation of scattering from an asymmetrically cut crystal. The crystal surface makes an angle α with the atomic planes which are parallel to the dotted lines. For a ray to be reflected, the scattering vector $\mathbf{q} \equiv \mathbf{k}_e - \mathbf{k}_i$ must fall along the segment of the crystal truncation rod with near-unit reflectivity T. The crystal truncation rod makes an angle of α with the reciprocal lattice vector $\mathbf{H}$.

Table 2
Bragg angles θ_B, angular widths w_i, w_e and angular offsets $\Delta\theta_i^{cen}$, $\Delta\theta_e^{cen}$ of various crystal reflections for an X-ray wavelength of $\lambda = 0.177$ nm (7.0 keV), σ polarization and both $b = -1$ and $b = -10$.

	Si(111)		Si(220)		Diamond(111)	
	$b = -1$	$b = -10$	$b = -1$	$b = -10$	$b = -1$	$b = -10$
θ_B (°)	16.40		27.45		25.46	
w_i (μrad)	−19.6	−6.2	−15.1	−4.8	−14.2	−4.5
w_e (μrad)	−19.6	−62.1	−15.1	−47.8	−14.2	−45.0
$\Delta\theta_i^{cen}$ (μrad)	36.3	20.0	24.0	13.2	38.3	21.1
$\Delta\theta_e^{cen}$ (μrad)	36.3	200.0	24.0	132.0	38.3	211.0

where we have treated the incidence and exit sides separately. The case of $\Delta\theta_i = \Delta\theta_e = 0$ is Bragg's law. For a given wavelength, the region of near-unit reflectivity is determined by

$$\Delta\theta_i^{cen} - w_i \leq \Delta\theta_i \leq \Delta\theta_i^{cen} + w_i, \tag{18}$$

$$\Delta\theta_e^{cen} - w_e \leq \Delta\theta_e \leq \Delta\theta_e^{cen} + w_e. \tag{19}$$

These ranges are themselves functions of wavelength and are typically smaller than 100 μrad, so that the region of near-unit reflectivity can be distinguished from the Bragg-law curves only in the enlarged views of Fig. 3. Since only those angles and wavelengths which fall within this region can be reflected by the crystal, we shall call this region the 'reflectivity band'. For the Bragg geometry, the upper and lower edges of the incident reflectivity band map onto the upper and lower edges, respectively, of the exit reflectivity band. The dashed line represents monochromatic, divergent incident illumination. From the intersection of the dashed line with the incident reflectivity band and its mapping across to the exit side, one can see that the exit Darwin width is $|b|$ times as large as the incident Darwin width. Likewise, if the divergence of the incident beam D_i only partially fills the incident Darwin width, the divergence of the exit beam will be $D_e = |b|D_i$.

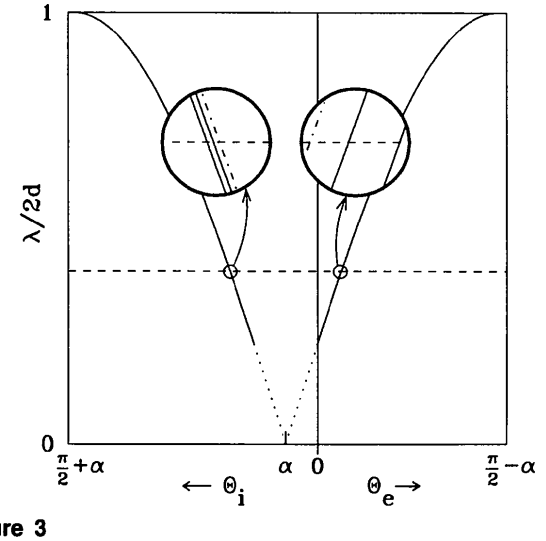

Figure 3
Schematic DuMond diagram for an asymmetrically cut crystal in the Bragg geometry. The horizontal dashed line represents divergent monochromatic radiation incident on the crystal. The enlarged insets show the Bragg-law curves (dot-dashed) and the reflectivity bands (between the solid lines) on the incidence and exit sides. The angular range emitted is $|b|$ times the angular range accepted.

4.2. *Polychromatic source*

In addition to providing a simple description of how monochromatic radiation is affected by an asymmetrically cut crystal, the DuMond diagram can also be used to treat the case of polychromatic illumination. For simplicity, consider first the case of perfectly collimated polychromatic radiation illuminating the crystal, which is a good approximation to the case of coherent X-ray beams. The description of this case on the incidence side of the DuMond diagram is obvious. The available rays within the source are represented by a vertical line as shown in Fig. 4. The intersection of this line with the incidence reflectivity band gives the wavelengths which will be passed by the crystal. Equation (14) shows how this intersection maps to the exit side. The vertical line on the incidence side of the DuMond

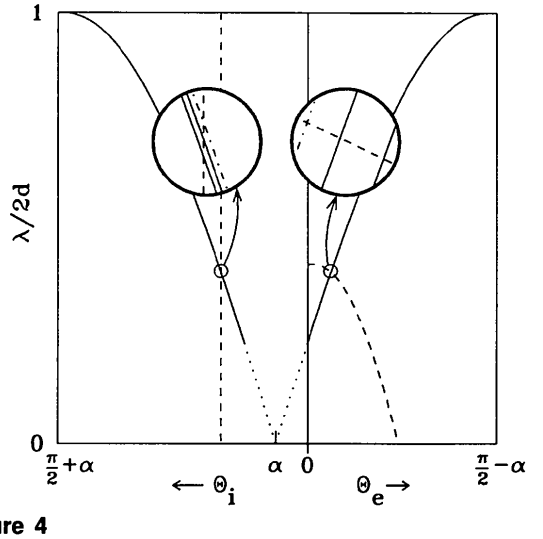

Figure 4
Schematic DuMond diagram for an asymmetrically cut crystal illuminated with perfectly collimated polychromatic radiation. The incident radiation is represented by the vertical dashed line which is transformed to the dashed cosine curve on the exit side. The enlarged insets show the Bragg-law curves (dot-dashed) and the reflectivity bands (between the solid lines) on the input and exit sides. As shown in the exit-side inset, the exit angular range is nearly the full Darwin width, even though the incident radiation is perfectly collimated.

diagram (θ_i fixed) is transformed to a cosine curve on the exit side. The intersection of this curve with the exit reflectivity band reveals the notable result that the exit divergence is nearly the full exit Darwin width, even though we began with perfectly collimated radiation. Moreover, the wavelength range is dispersed across the exit-angle range. The full ranges of wavelengths and exit angles are given by the simple relations

$$\Delta\lambda/\lambda = 2|w_i|/\tan\theta_B, \tag{20}$$

$$D_e = 2|w_i - w_e| = 2|w_i|\,|1 + b|. \tag{21}$$

(Recall that w_i, w_e and b are all negative in the Bragg geometry.)

The extension of the DuMond analysis to the case of a polychromatic source with a finite angular divergence is straightforward. If we imagine two closely spaced vertical lines on the input side of Fig. 4, which define the range of incidence angles, these map into two closely spaced cosine curves on the exit side. Thus, there are parallelograms of intersection on the incident and exit side, which define the wavelengths and angles accepted and emitted by the crystal, respectively. For an incident divergence D_i, the full ranges of wavelengths and exit angles are now given by

$$\Delta\lambda/\lambda = (2|w_i| + D_i)/\tan\theta_B, \tag{22}$$

$$D_e = 2|w_i||1 + b| + D_i. \tag{23}$$

The behavior depends on the size of the incident divergence D_i compared with the incident Darwin width $2|w_i|$. When the incident divergence is large ($D_i >> 2|w_i|$), the exit divergence is equal to the incident value. When the incident divergence is small ($D_i << 2|w_i|$), the exit divergence approaches the lower limit set by (21). At the crossover point $D_i = 2|w_i|$, the exit divergence is given by $D_e = |b|D_i$ for $b < -1$. Only under this condition is the exit divergence for a polychromatic beam as small as it would be for a monochromatic beam.

Note that in the special case of $b = -1$, the exit divergence given by (23) is always equal to the incident divergence. This illustrates the unique property of symmetric Bragg reflection: the beam divergence is unaltered upon reflection because $\theta_i = \theta_e$ for all λ.

5. Matsushita–Kaminaga formalism

5.1. *Radiation passing through a pinhole*

The matrix formalism developed by Matsushita & Kaminaga (1980), hereafter referred to as the M–K formalism, permits a more general treatment of the wavelengths and angles transmitted through a sequence of crystals and apertures. We will use the M–K formalism to examine in detail the situation where a pinhole aperture is located a distance L_e downstream from a flat asymmetrically cut crystal in order to select a beam from a real synchrotron source. This situation is illustrated in Fig. 5. The crystal itself is a distance L_i from the source of size A. For those rays which pass through the pinhole, the divergence on the incident side of the crystal is not known *a priori*, so that it is necessary to trace the rays from the pinhole back to the source, accounting for their *spatial* as well as angular and wavelength coordinates.

To conduct the ray tracing in this approach, we consider small variations about the central operating point, in space (y), angle (y') and wavelength ($\Delta\lambda/\lambda$). The position, angle and wavelength coordinates of rays in the source $\mathbf{y}_s = (y_s, y'_s, \Delta\lambda/\lambda)$ are transformed to those at the pinhole $\mathbf{y}_p = (y_p, y'_p, \Delta\lambda/\lambda)$ by the product of three transfer matrices thus:

$$\mathbf{y}_p = \mathbf{T}_e\mathbf{T}_{\rm cryst}\mathbf{T}_i\mathbf{y}_s, \tag{24}$$

where

$$\mathbf{T}_i = \begin{bmatrix} 1 & L_i & 0 \\ 0 & 1 & 0 \\ 0 & 0 & 1 \end{bmatrix} \text{ and } \mathbf{T}_e = \begin{bmatrix} 1 & L_e & 0 \\ 0 & 1 & 0 \\ 0 & 0 & 1 \end{bmatrix} \tag{25}$$

map the evolution of the rays from the source to the crystal and the crystal to the pinhole, respectively, and

$$\mathbf{T}_{\rm cryst} = \begin{bmatrix} 1/b & 0 & 0 \\ 0 & b & -(1+b)\tan\theta_B \\ 0 & 0 & 1 \end{bmatrix} \tag{26}$$

is the transfer matrix of the crystal. [Note that Matsushita & Kaminaga chose to invert their coordinate system upon reflection from a Bragg crystal in order that the angle y' of a given ray has the same sign both before and after reflection, as is conventional for incidence (θ_i) and exit (θ_e) angles. However, in the treatment of optical systems where multiple matrices are required to conduct the ray tracing, it is more convenient to have a single absolute sense for all ray angles. We have adopted the latter convention. In our M–K formalism therefore, $y'_s = \Delta\theta_i$ while $y'_p = -\Delta\theta_e$.]

Properties of the radiation passing through the pinhole may be found by seeking solutions to (24) where y_p is on either side of the pinhole diameter Z, and y_s is on either side of the source of size A. Each of these combinations ($y_s = \pm Z/2$, $y_p = \pm A/2$) gives a line of $\Delta\lambda/\lambda$ *versus* $y'_p = -\Delta\theta_e$ in M–K space. The four lines together bound a region of rays which would pass through the pinhole

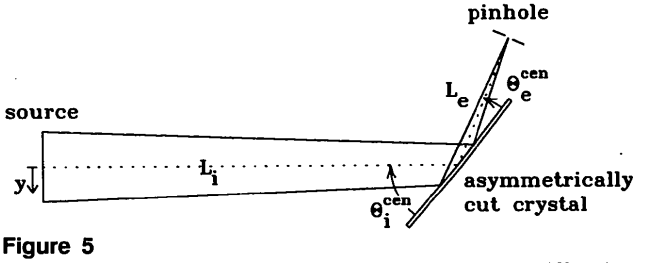

Figure 5
Geometry of rays leaving a finite-size X-ray source, diffracting from an asymmetrically cut crystal and entering a pinhole aperture.

provided they are reflected by the crystal. Because of the close relationship with the geometry of the source and apertures in the system, we will refer to the region bounded by these lines as the 'geometrical band' on the exit side. These negatively sloped lines are shown in Fig. 6, which is essentially a small region from a DuMond diagram.

To incorporate the reflectivity band of the crystal, (17) is linearized around the operating point resulting in the two solid lines in Fig. 6. These lines

$$(\Delta\lambda/\lambda)\tan\theta_B = \Delta\theta_e \pm w_e, \tag{27}$$

delimit the exit reflectivity band.

From the intersection of the geometrical band with the reflectivity band, the wavelength range and exit divergence are found to be:

$$\frac{\Delta\lambda}{\lambda} = \frac{2|w_i|(L_i + b^2L_e) + A + |b|Z}{(L_i - bL_e)\tan\theta_B} \tag{28}$$

$$D_e = \frac{2|w_i||1 + b|L_i + A + |b|Z}{L_i - bL_e}. \tag{29}$$

As shown in Fig. 6 these quantities are the extreme widths, measured from the projection of the most extreme points on the M–K parallelepiped of transmitted rays. There are three separate contributions to the wavelength and exit-angle ranges, as can be seen from the numerators of (28) and (29). The first of these is due to the Darwin width of the crystal $2|w_i|$. In the case of $L_i \to \infty$ this term dominates the others and equations (28) and (29) reduce to our results for perfectly collimated incident radiation, equations (20) and (21). The second term arises from the finite source size A while the third term is due to the finite size of the pinhole aperture Z. In the case of $L_e = 0$, equations (28) and (29) reduce to equations (22) and (23), where the second and third terms give the incident divergence D_i. All three terms in equations (28) and (29) are positive because each of these effects broadens the angle and wavelength range. Although the three terms add linearly to give the extreme width, the FWHM values for the wavelength spread and exit divergence might be better approximated by adding these terms in quadrature. Note that if $L_i = bL_e$, which can happen in the Laue case, both $\Delta\lambda/\lambda$ and D_e diverge. This is due to the 'focusing' property of a Laue crystal whereby rays that leave a point source and diffract from the crystal converge to another point.

Figs. 7(*a*) and 7(*b*) show $\Delta\lambda/\lambda$ and D_e as functions of L_e for various asymmetry factors, in conditions typical of our experiments at X25. From Fig. 7(*a*) we see that at $L_e = 0$, the wavelength range decreases with increasing asymmetry, owing to the reduction in $|w_i|$. In addition, the wavelength spread is a sensitive function of L_e for large asymmetry factors. For example, by changing L_e from 0.1 to 0.5 m with the $b \simeq -10$ crystal of our experiments, $\Delta\lambda/\lambda$ is increased by a factor of almost 2. The same change in L_e has a smaller effect on the divergence. However, Fig. 7(*b*) shows that D_e is abruptly increased as we change from a symmetric surface ($b = -1$) to even a small asymmetry. Unfortunately, the maximum increase of 7× in D_e that we

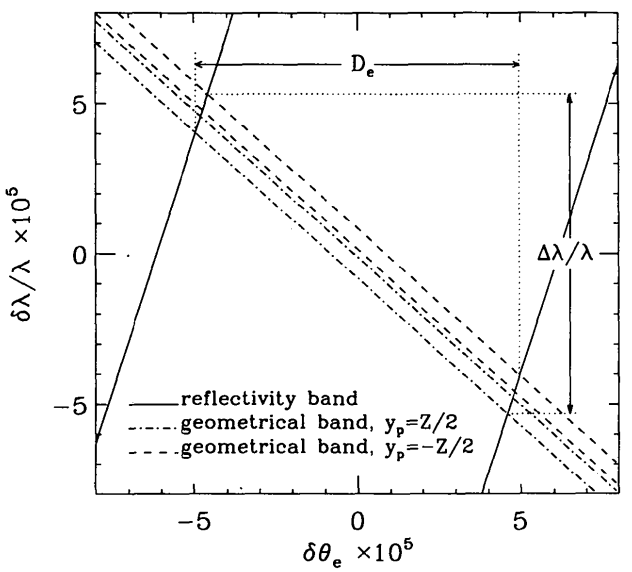

Figure 6
M–K space diagram showing the range of wavelengths and angles passing through a $Z = 7\,\mu$m pinhole aperture after reflection from an asymmetrically cut crystal. The reflectivity band is drawn for Si(111) ($d = 0.3135$ nm) with a miscut angle of $\alpha = 13.5°$, and X-ray wavelength of $\lambda = 0.177$ nm (7.0 keV). At this wavelength, the asymmetry factor is $b = -9.83$ and the exit Darwin width is $2|w_i| = 123\,\mu$rad. The geometrical band is drawn for NSLS beamline X25, where $L_i = 27.3$ m, $L_e = 0.438$ m and $A = 50\,\mu$m.

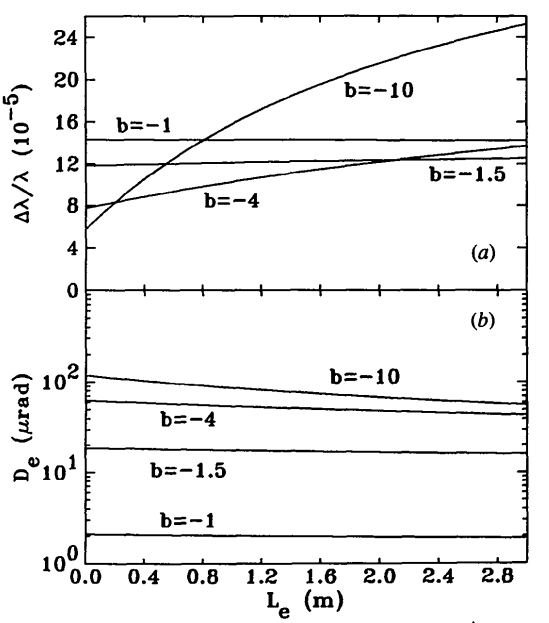

Figure 7
Wavelength range (*a*) and exit divergence (*b*) of radiation passing through a $Z = 7\,\mu$m pinhole aperture, as a function of crystal–pinhole separation L_e, for various asymmetry factors b. As for the NSLS wiggler beamline X25, the X-ray source has height $A = 50\,\mu$m and is located $L_i = 27.3$ m from the asymmetric Si(111) crystal. The wavelength is $\lambda = 0.177$ nm (7.0 keV).

Table 3
Size and flux of transversely coherent X-ray beams obtained using a horizontal aperture at the source, a vertically diffracting Si(111) crystal of asymmetry b, and a pinhole aperture, for wavelength $\lambda = 0.177$ nm, $L_i = 27.3$ m, $L_e = 0$ and source brilliance $B = 1\times10^{15}$ photons s^{-1} mm^{-2} mrad^{-2} (0.1% bandwidth)$^{-1}$.

Horizontal transverse			Vertical transverse						Long.			
A^{hor} (μm)	D^{hor} (μrad)	d_t^{hor} (μm)	A (μm)	D_i (μrad)	b	$2\|w_i\|$ (μrad)	D_e (μrad)	d_t (μm)	$\Delta\lambda/\lambda$ (10^{-6})	$Z^{hor}\times Z$ (μm)	F_t (10^6 counts s^{-1})	F_t/F_t^{max}
1000	36.6	2.4	50	1.8	−1	39	1.8	48	140	2.4×48	1.04	0.96
1000	36.6	2.4	50	1.8	−1	39	1.8	48	140	2.4×2.4	0.052	0.048
345	12.6	7.0	50	1.8	−1	39	1.8	48	140	7.0×7.0	0.152	0.14
50	1.8	48	50	1.8	−1	39	1.8	48	140	48×48	1.04	0.96
345	12.6	7.0	50	1.8	−1.32	34	12.6	7	122	7.0×7.0	0.173	0.18
1000	36.6	2.4	50	1.8	−2.36	26	36.6	2.4	93	2.4×2.4	0.082	0.109

can tolerate occurs at the slight asymmetry of $b = -1.3$, which offers only a modest increase in coherent flux, as described in the next section.

6. Optimization of coherent X-ray beams

As discussed in the introduction, our goal is to produce a transversely coherent X-ray beam of desired size and monochromaticity which is as intense as possible. When the desired size is smaller than the transverse coherence length in the incident beam, an asymmetrically cut crystal can be used as shown in Fig. 5 to condense the beam spatially, increasing the flux coming through the beam-defining pinhole. The optimum asymmetry and flux are determined by the maximum exit divergence that can be tolerated without reducing the transverse coherence length below the desired size.

We begin by developing expressions for the flux in a coherent beam. If we first consider a beam with no correlation between position, angle and wavelength, the flux through a given pinhole area $Z^{hor}\times Z^{vert}$ is simply the product of the beam brilliance B and the accepted area, solid angle and wavelength range, $F = Z^{vert}D^{vert}Z^{hor}D^{hor}(\Delta\lambda/\lambda)B$. For a coherent beam, where the pinhole dimensions have been set to equal the transverse coherence lengths $Z = d_t \equiv \lambda/2D$, one obtains

$$F_t^{max} = \left(\frac{\lambda}{2}\right)^2 \frac{\Delta\lambda}{\lambda} B. \qquad (30)$$

The coherent flux is thus proportional to the brilliance and independent of the transverse coherence length. Although optics can be used to modify d_t, the brilliance of the beam cannot be increased. This formula thus gives the maximum coherent flux that can be obtained within a given wavelength range at any d_t.

For a monochromatic beam, a crystal of large Darwin width $2|w_i| > D_i$, cut with asymmetry b, produces an exit beam with $Z_e = Z_i/|b|$ and $D_e = |b|D_i$, with the product $Z_eD_e = Z_iD_i$ remaining constant. Thus, for a monochromatic beam, an asymmetric crystal can be used to modify the transverse coherence length while preserving the coherent flux.

For a non-monochromatic beam, an asymmetric crystal in general introduces a correlation between the wavelength and the exit angle and position in the diffraction direction. This causes the useful coherent flux in a given $\Delta\lambda/\lambda$ to be smaller than the maximum value. The flux through a pinhole of vertical size Z is given by

$$F = \left(\frac{|b|ZA}{L_i - bL_e}\frac{2|w_i|}{\tan\theta_B}\right) Z^{hor}D^{hor}B \qquad (31)$$

where we have assumed the diffraction plane to be vertical. The factor in parentheses is the position–angle–wavelength volume of the M–K space parallelepiped accepted by the crystal–pinhole system, calculated using the analysis in §5.

The flux that can be obtained in transversely coherent beams of various sizes is shown in Table 3, for source parameters typical of NSLS wiggler beamline X25 and using an Si(111) reflection. For this table, a value of $L_e = 0$ has been used and the contribution of finite pinhole size has been neglected, so that equations (22) and (23) can be used to calculate $\Delta\lambda/\lambda$ and D_e, with $D_i = A/L_i$. In the upper section of the table, the behavior of a symmetrically cut crystal is shown for comparative purposes. The first row gives the results using the full source size of 1000×50 μm and a symmetrically cut crystal. The factor of 20 difference in the source dimensions leads to unequal horizontal and vertical transverse coherence lengths of 2.4×48 μm. The transversely coherent flux F_t obtained by using a pinhole with these dimensions, calculated using (31), is shown in Table 3. Because the symmetrically cut crystal introduces almost no correlation between angle and wavelength, the coherent flux is nearly equal to the maximum possible coherent flux.

To obtain a coherent beam with equal horizontal and vertical dimensions, one can simply use a circular pinhole with diameter given by the smaller of the two transverse coherence lengths. This is demonstrated in the second row, columns 11–13, of the Table 3. In this case the flux obtained in a 2.4 μm square beam is a factor of 20 below the optimum.

If the desired beam size is larger than the 2.4 μm coherence length obtained using the full horizontal source size, it is useful to put a horizontal aperture near the source

which effectively reduces the source size $A^{\rm hor}$ and increases $d_t^{\rm hor}$ to the desired beam size. The flux in equiaxial 7 and 48 μm coherent beams is shown in rows 3 and 4 of the table. Such an aperture near the source is a very effective way to increase the coherence length controllably. In particular, the maximum possible coherent flux is obtained in an equiaxial 48 μm beam simply by reducing the effective source size in the horizontal to be equal to that in the vertical.

The improvement in coherent flux that can be obtained using an asymmetrically cut crystal is shown in the lower section of the table. For beam sizes of 7.0 and 2.4 μm, the optimum asymmetry is that which increases the exit divergence to the maximum allowable value to preserve coherence, *i.e.* 12.6 and 36.6 μrad, respectively. Because of the rapid increase in exit divergence with only small departures from the symmetric geometry, given by (23), only very modest improvements in coherent flux can be obtained in this example. Increases in D_e by factors of 6.9 and 20 are produced using asymmetries which condense the beam size by factors of $|b| = 1.32$ and 2.36, respectively. Because $\Delta\lambda/\lambda$ is also decreased by a factor of $|b|^{1/2}$, the coherent flux is increased only by factors of 1.15 and 1.54, respectively. The fundamental reason why the asymmetric crystal is only marginally effective in improving the coherent flux is that the collimated polychromatic incident beam is dispersed across the exit Darwin width, as shown in Fig. 6.

Although in this example we have considered only a Si(111) reflection, the results obtained depend strongly upon the crystal and reflection chosen. For the problem considered, the main effect of using a higher-index Si peak (220, 004, *etc.*) is to decrease the wavelength range $\Delta\lambda/\lambda$ (and therefore the flux) considerably while improving $F_t/F_t^{\rm max}$ only marginally. In general, the type of crystal and its properties (Ψ_H, $\tan\theta_{\rm B}$, b) can be optimized given the requirements of the problem (D_i, $\Delta\lambda/\lambda$, Z). For example, the ratio of the coherent flux to the maximum coherent flux $F_t/F_t^{\rm max}$ depends upon the ratio of the incident divergence to the incident Darwin width $D_i/2|w_i|$. In particular, when the latter ratio is unity, the former is always 1/2 [using $L_e = 0$ and neglecting the terms containing Z in (28) and (29)]. Thus, a good choice of crystal and reflection for current purposes will have $2|w_i|$ approximately equal to D_i. Another consideration is the wavelength range $\Delta\lambda/\lambda$ desired, which depends upon the (generally conflicting) requirements for longitudinal coherence and flux. If a given D_i determines $2|w_i|$, then a desired $\Delta\lambda/\lambda$ can be obtained by choosing a crystal with an appropriate value of $\tan\theta_{\rm B}$. For the problem considered above, crystals with smaller values of both $\tan\theta_{\rm B}$ and Ψ_H would in principle give better results.

7. Comparison with experiment

An experiment was conducted at NSLS beamline X25 to measure the effect of an asymmetrically cut crystal on the divergence and flux obtained through a pinhole aperture. A pair of flat Si(111) symmetric Bragg crystals in non-dispersive configuration were used in the beamline monochromator, which was set to $\lambda = 0.177$ nm (7.0 keV). A third symmetric Si(111) crystal and the crystal under study [Si(111) cut to $\alpha = 13.5$ or 0° giving $b = -10$ or -1, respectively] were placed within the experimental hutch, again in a nondispersive configuration, the latter crystal being downstream. All crystals were vertically diffracting (σ polarization). A pinhole aperture was placed at $L_e = 0.438$ m downstream of the final crystal. Since the three upstream symmetrically cut crystals did not alter the divergence of the beam and since they transmitted an angular range at least as wide as the incident Darwin width $2|w_i|$ of the final crystal, they did not substantially alter the bandpass, divergence or flux through the pinhole. The crystals were aligned in the χ-direction (rotation along the incident beam axis) to ±0.05° to obtain maximum throughput. (The crystals had been prepared by Semiconductor Processing Company, 409 East 1st St, Boston, MA 02127, USA. Crystal quality was measured at $\lambda = 0.154$ nm, where the $\alpha = 13.5°$ crystals have $b = -36.9$. The narrow Darwin width was measured by rocking one such crystal against another, both being mounted in a strain-free fashion. The rocking curve had a width of 8.0 ± 0.5 μrad which agrees with the theoretical value of 7.6 μrad.) The pinhole apertures were manufactured (Optimation Inc., Windham, NH 03087, USA) by pulsed laser drilling through 50 μm-thick platinum foils. The source size at X25 was estimated by scanning a slit across the beam 10 m downstream from the source, and monitoring the intensity transmitted by a pinhole aperture in the experimental hutch. The source was found to be 43 μm FWHM high, which is close to the designed source size of 50 μm.

Fig. 8 shows the measured angular distribution of X-rays exiting a $Z = 18$ μm diameter pinhole, after diffracting

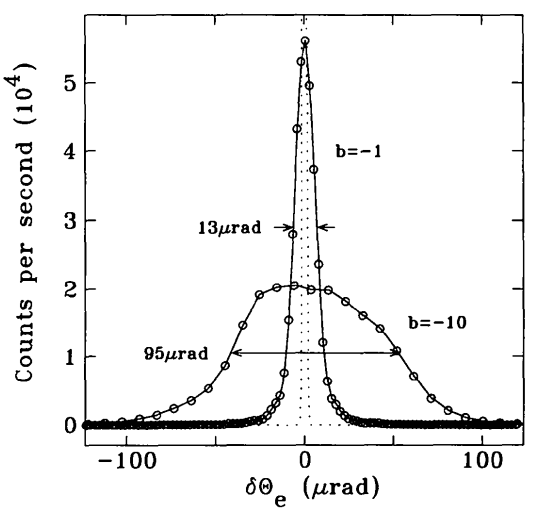

Figure 8
Angular distribution of X-rays exiting an 18 μm diameter pinhole, after vertically diffracting from Si(111) with $b = -1$ and $b = -10$. The dotted curve shows the calculated divergence (1.8 μrad) for $b = -1$, under the experimental conditions of $L_i = 27.3$ m, $L_e = 0.438$ m and $A = 50$ μm.

from Si(111) crystals with $b = -1$ or $b = -10$. The data were acquired by vertically scanning a 7 μm diameter detector aperture located 1 m behind the beam-defining pinhole. The symmetric case ($b = -1$) was included in order to verify the resolution of the measurement. The dotted curve is the calculated distribution for $b = -1$ in the absence of pinhole diffraction and resolution broadening. From the estimated source size of $A = 50\,\mu m$, the calculated full width is $A/(L_i + L_e) = 1.8\,\mu rad$. The measured curve for $b = -1$ has a FWHM of 13 μrad. This width is dominated by Fraunhoffer diffraction from the pinhole itself, which contributes $\lambda/Z = 10\,\mu rad$ and by the resolution of the measurement (7 μrad). The measured angular distribution for the asymmetric case ($b = -10$) is clearly much broader than the pinhole diffraction plus resolution. The measured FWHM of 95 μrad for $b = -10$ is consistent with the extreme width of 104 μrad calculated using (29). It is more than a factor of 50 larger than the incident divergence of 1.8 μrad. Thus, our measurement verifies that the divergence of the incident beam is broadened by much more than a factor of $|b| = 10$ due to the behavior of an asymmetrically cut crystal in a polychromatic beam.

The total flux through the $Z = 7\,\mu m$ pinhole was measured for both $b = -1$ and $b = -10$ by using a large-diameter detector aperture to capture all radiation transmitted through the pinhole. For the selected horizontal source size ($A^{hor} = 1.1$ mm) and a ring current of 200 mA, we observed 4.2×10^5 counts s^{-1} with $b = -1$ and 1.1×10^6 counts s^{-1} with $b = -10$. The measured flux enhancement is also evident from the integrated areas of Fig. 8. These flux measurements are in good agreement with (31), which predicts a flux enhancement of 2.7× for this geometry.

8. Conclusions

We have investigated in detail the relationship between incident angle, exit angle and wavelength for diffraction of X-rays from crystals in the asymmetric Bragg geometry. The results of dynamical diffraction theory for perfect crystals can be concisely described in reciprocal space, using the concept of a crystal truncation rod. We have used these results to understand how X-ray beams which are polychromatic yet highly collimated are diffracted from asymmetrically cut crystals. It is found that the angular range in the exit beam is typically dispersed across the full exit Darwin width, even if the incident beam is perfectly collimated. This effect can be viewed as a strong chromatic aberration, whereby the wavelength spread accepted by the crystal is transformed into an angular spread. Only the symmetric Bragg geometry is free from this aberration. For an asymmetrically cut crystal, the only condition under which the exit divergence for a polychromatic beam is as small as that for a monochromatic beam is when the incident divergence is equal to the incident Darwin width, $D_i = 2|w_i|$.

For the case of a pinhole collimator located after an asymmetrically cut crystal, we have determined the range of wavelengths and angles which are transmitted. We investigated the possibility of using this geometry to increase the flux in a coherent X-ray beam. In the specific example considered, we found that the divergence is increased to a far greater extent than the beam is spatially condensed, so that the transverse coherence length is greatly reduced and the coherent flux is not conserved. A consequence of this effect is that only crystals cut to a slight asymmetry could be used, providing only a modest increase in usable coherent flux.

We would like to thank Ralf Brüning and Eric Dufresne for their assistance with the experiments and Lonny E. Berman and Denis T. Keane for their comments on the manuscript. The experiments were conducted at beamline X25, NSLS, which is operated under the United States Department of Energy contract DE-AC02-76CH00016. This research was supported in part by the Natural Sciences and Engineering Research Council of Canada.

APPENDIX
Crystal truncation rods and dynamical diffraction theory

The relationship between the dispersion surface diagram and the crystal truncation rod (CTR) is shown in Fig. 9. While it is most convenient to use a dispersion surface diagram to derive dynamical diffraction theory for perfect crystals with an arbitrarily oriented surface, the resulting diffraction behavior is most clearly described using the concept of a CTR in reciprocal space. The reader is referred to Batterman & Cole (1964) for a complete description of dynamical theory and dispersion surfaces. Note that all

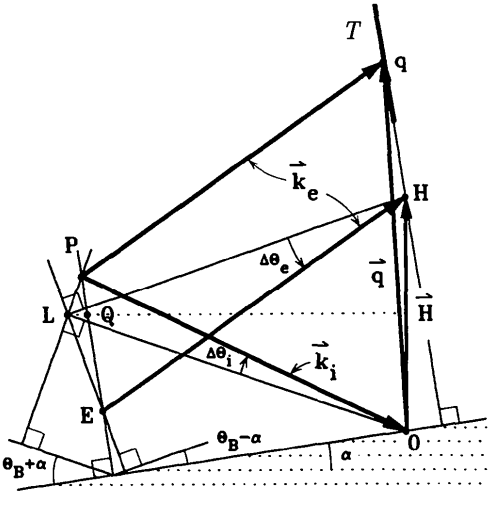

Figure 9
Reciprocal-space representation of dynamical diffraction showing the relationship between the dispersion-surface construction used by Batterman & Cole and the crystal truncation rod used to describe surface diffraction.

of the results of interest here, except the exact width of the reflection, can be obtained simply by considering the refractive index correction to kinematical theory.

The vector **H** is the reciprocal lattice vector of interest. The orientation of the crystal lattice planes for this reflection is shown by the dotted lines. The length of **H** is $2\pi/d$. The point L is the center of the Ewald sphere in the simplest kinematical diffraction theory, which gives Bragg's law (1). In this approximation the lines LO and LH, both of length $2\pi/\lambda$, represent the incident and exit wavevectors, respectively. They each make an angle θ_B with respect to the lattice planes.

When kinematical theory is modified to account for the refractive index of the crystal, there are two important changes. Firstly, the X-ray wavelength inside the crystal is slightly longer than its value λ outside because the real part of the refractive index of the crystal $\mathrm{Re}(n)$ is less than unity by the small amount

$$\delta \equiv 1 - \mathrm{Re}(n) = \lambda^2 \frac{|F_0|}{|F_H|} \frac{\Psi_H}{4d^2}. \qquad (32)$$

The center of the Ewald sphere thus shifts inward from L to Q, the magnitude of the shift being greatly exaggerated in Fig. 9 for clarity. With this modification the lines QO and QH, both of length $2\pi\mathrm{Re}(n)/\lambda$, represent the incident and exit wavevectors, respectively, inside the crystal.

Secondly, the directions of the incident and exit beams outside the crystal differ from those inside because of refraction at the surface. The crystal surface orientation is shown at the bottom of the figure, making an angle α with respect to the diffracting planes. The construction shown in Fig. 9 can be used to show that the incident and exit wavevectors outside the crystal, $\mathbf{k}_i$ and $\mathbf{k}_e$, are given by PO and EH, respectively. This construction is based on the principle which leads to Snell's law, *i.e.* that the wavevectors outside the crystal can differ from those inside only by a component normal to the crystal surface. In addition, the length of the outside wavevectors must be the same as LO and LH. To satisfy these two criteria, one can construct lines passing through L perpendicular to LO and LH that represent small arcs centered on O and H having radii of the correct length. The intersections P and E of these lines with the line drawn through Q normal to the crystal surface give the endpoints of the outside wavevectors PO and EH which correctly match the inside wavevectors QO and QH, respectively.

The scattering vector $\mathbf{q} \equiv \mathbf{k}_e - \mathbf{k}_i$ given by this construction can be obtained simply by translating the exit wavevector from E to P, as shown in Fig. 9. One can see that the tip q of the scattering vector **q** is displaced slightly from the reciprocal lattice point H in a direction normal to the crystal surface, owing to the effect of the refractive index of the crystal.

So far we have neglected the finite width of the reflection predicted by dynamical diffraction theory. In the dynamical theory as described by Batterman & Cole (1964) (neglecting absorption), the point Q becomes the center of an approximately hyperbolic dispersion surface which defines the loci of allowed centers of Ewald spheres inside the crystal. The finite diameter of this hyperbola gives rise to the finite width of the reflection in the Bragg geometry. The construction shown in Fig. 9 remains valid, with the vectors $\mathbf{k}_i$, $\mathbf{k}_e$ and **q** as drawn corresponding to the center of the reflection. All allowed scattering vectors which have significant diffracted intensity terminate on the line segment T in reciprocal space. The line segment T is centered on q and oriented normal to the crystal surface. Allowed scattering vectors can differ from **H** only by vectors normal to the surface because of the boundary conditions relating wavevectors inside and outside the crystal.

By representing the results of dynamical theory in reciprocal space, we can see how they are directly related to the crystal truncation rod (CTR) used to describe diffraction from crystal surfaces. According to a kinematical approach (Robinson, 1986), such CTRs arise when the crystal is truncated by a surface. The CTR lies along the line through H normal to the surface and represents all of the allowed scattering vectors for the reflection. The line segment T is the section of the CTR with near-unit reflectivity. The length and location of T, deduced from dynamical theory and the geometry of Fig. 9, are given at the end of §3.

References

Batterman, B.W. & Cole, H. (1964). *Rev. Mod. Phys.* **36**, 681–717.

Brauer, S., Stephenson, G. B., Sutton, M., Brüning, R., Dufresne, E., Mochrie, S. G. J., Grübel, G., Als-Nielsen, J. & Abernathy, D. L. (1995). *Phys. Rev. Lett.* **74**, 2010–2013.

Brauer, S., Stephenson, G. B., Sutton, M., Mochrie, S. G. J., Dierker, S. B., Fleming, R. M., Pindak, R., Robinson, I. K., Grübel, G., Als-Nielsen, J. & Abernathy, D. L. (1995). *Rev. Sci. Instrum.* **66**(2), 1506–1509.

Caciuffo, R., Melone, S., Rustichelli, F. & Boeuf, A. (1987). *Phys. Rep.* **152**, 1–71.

Dufresne, E., Brüning, R., Sutton, M., Stephenson, G. B., Rodricks, B., Thompson, C. & Nagler, S. E. (1992). *NSLS Annual Report*. BNL 52317, p. 381. Brookhaven National Laboratory, USA.

DuMond, J. W. M. (1937). *Phys. Rev.* **52**, 872–883.

Ishikawa, T. (1988). *Acta Cryst.* A**44**, 496–499.

Kuriyama, M. & Boettinger, W. J. (1975). *Acta Cryst.* A**32**, 511–512.

Matsushita, T. & Hashizume, H. (1983). *Handbook on Synchrotron Radiation*, Vol. 1*A*, edited by E. E. Koch, pp. 261–314. Amsterdam: North Holland.

Matsushita, T. & Kaminaga, U. (1980). *J. Appl. Cryst.* **13**, 465–471; 472–478.

Robinson, I. K. (1986). *Phys. Rev. B*, **33**, 3830–3836.

Sutton, M., Mochrie, S. G. J., Greytak, T., Nagler, S. E., Berman, L. E., Held, G. A. & Stephenson, G. B. (1991). *Nature (London)*, **352**, 608–610.